Journal of Membrane Science and Research 6 (2020) 70-80

Journal of Membrane Science & Research

journal homepage: www.msrjournal.com

Research Paper

The Ultrafiltration Performance of Cellulose Acetate Asymmetric Membranes: A New Perspective on the Correlation with the Infrared Spectra

Ana Sofia Figueiredo [1,2], Ana Rosa Garcia [3,4], Miguel Minhalma [1,2], Laura Ilharco [3], Maria Norberta de Pinho [1,*]

[1] *CeFEMA/Department of Chemical Engineering, Instituto Superior Técnico, Universidade de Lisboa, Av. Rovisco Pais, 1, 1049-001 Lisbon, Portugal*
[2] *Departmental Area of Chemical Engineering, Instituto Superior de Engenharia de Lisboa, Instituto Politécnico de Lisboa, Rua Conselheiro Emídio Navarro 1, 1959-007 Lisbon, Portugal*
[3] *Centro de Química-Física Molecular and IBB - Institute for Bioengineering and Biosciences, Instituto Superior Técnico, Universidade de Lisboa, Av. Rovisco Pais 1, 1049-001 Lisboa, Portugal*
[4] *Departamento de Química e Farmácia, FCT, Universidade do Algarve, Campus de Gambelas, 8005-139 Faro, Portugal*

Article info

Received 2019-06-29
Revised 2019-09-24
Accepted 2019-09-28
Available online 2019-09-28

Keywords

Ultrafiltration
Cellulose acetate
Salts rejection
ATR-FTIR
Water structures

Highlights

- ATR-FTIR assessment of UF membranes surfaces
- Water structure in the membrane surface varies with the membrane pore size
- UF capability for differentiating anionic species is enabled, like in NF membranes

Graphical abstract

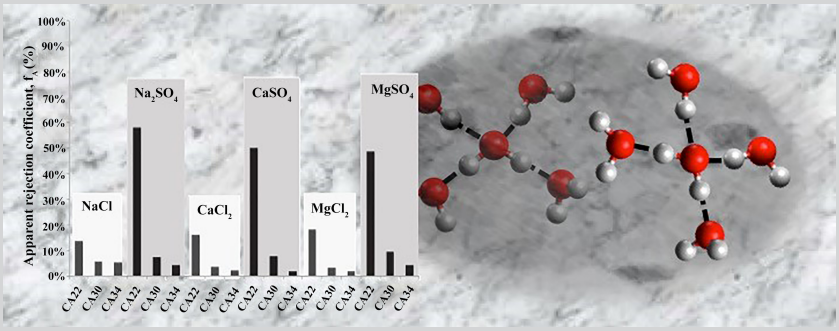

Abstract

Integral asymmetric cellulose acetate (CA) membranes have been casted by phase-inversion with formamide varying content - 22, 30 and 34% - as pore promoter. These membranes, CA-22, CA-30 and CA-34, were analysed by infrared spectroscopy in attenuated total reflection mode (ATR-FTIR) to investigate the porous membrane matrix influence on the polymer/water/solute interactions and the selective ultrafiltration of salts. The membranes covered a wide range of hydraulic permeabilities, from 3.5 to 81.0 $kg.m^{-2}.h^{-1}.bar^{-1}$, and of molecular weight cut-offs, from 4.17 to 31.43 kDa. The experimental apparent rejection coefficients of neutral solutes of increasing molecular weight are related to their intrinsic rejection coefficients through the film model. The surface average pore radius, estimated by an iterative algorithm, ranges from 2.1 to 4.5 nm. The tighter membrane, CA-22, displays experimental apparent rejection coefficients to Na_2SO_4, $CaSO_4$, $MgSO_4$ of 50% or higher values and this is in contrast with the lower values, between 14 and 18%, to NaCl, $CaCl_2$ and $MgCl_2$ salts. The ATR-FTIR evidences that in the membranes with larger pores, CA-30 and CA-34, the water molecules are organized with a liquid-water-like structure, in which most molecules are hydrogen bonded to four or to two others; nevertheless, a fraction of water molecules is strongly bonded to the CA carbonyl groups. For the CA-22 membrane, there are more free carbonyl groups and a larger fraction of free water, both able to interact with solutes, such as the hydrated sulphate ions. Therefore, this ultrafiltration membrane has the capability of differentiating anionic species.

1. Introduction

The Loeb and Sourirajan [1] integrally skinned cellulose acetate (CA) membranes were a landmark on the large scale development of reverse osmosis (RO), nanofiltration (NF) and ultrafiltration (UF). The versatility introduced on the membrane preparation by the wet phase inversion method and on the formulation of the casting solutions was a strong asset on the tailoring of final asymmetric structures with active layers characterized by selective permeation properties in the range of UF, NF and RO [2-4]. Early investigation on the correlation of RO membrane selective permeation properties with the state of water in the membrane porous structure was carried out with thin dense symmetric CA membranes as representative models for the active layers of the integrally skinned CA membranes [5-10]. De Pinho et al. addressed this issue in the porous structure of the active layer

* Corresponding author at: Phone: +351 218417488; fax: + 351 218417246
E-mail address: marianpinho@tecnico.ulisboa.pt (M.N. de Pinho)

DOI: 10.22079/JMSR.2019.110424.1269

of integral asymmetric cellulose acetate membranes covering the range of pressure-driven processes from UF, NF to RO. They concluded that the lightly clustered water species, weakly hydrogen-bonded to the polymer hydroxyl groups, were associated to the less permeable membranes of RO, whereas the more permeable membranes of UF contain water characterized by strong hydrogen-bonding, with ability to hydrate ions and enable their permeation [4, 11-13]. The traditional association of UF with molecular sieving mechanisms is in many situations like protein ultrafiltration coupled with the contribution of electrostatic interactions [14-16]. In contrast with the large report of these electrostatic interactions, the literature is very scarce on the role of other interaction forces of the type of hydrogen bonding and their correlation to the UF selective convective permeation to salts. Taking into account the unique physical-chemical characteristics of CA and its capability of establishing hydrogen bonding interactions with water molecules and solutes, the present work addresses this issue through the systematic analysis of infrared spectra in attenuated total reflection mode (ATR-FTIR) in different porous structures of CA ultrafiltration asymmetric membranes.

2. Materials and methods

2.1. Membrane synthesis

The cellulose acetate (39.8% acetyl content, M_n ~ 30000, supplied by Aldrich) is schematically represented in Figure 1 (based on the general cellulose acetate structure [17]).

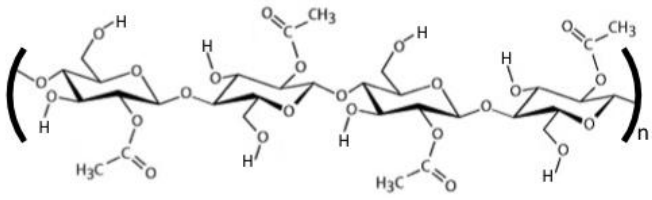

Fig. 1. Schematic representation of cellulose acetate the acetyl substitution was represented in order to respect the ~39.8% acetyl content.

The UF membranes were prepared by phase inversion using the wet process as described by Kunst and Sourirajan [18]. Table 1 shows the details of the casting solutions compositions and the casting conditions. The membranes are identified as CA (for cellulose acetate) followed by a number: 22, 30 or 34 for the wt% of formamide in the casting solution.

The top denser layer of each membrane will be named active layer (AL) and the support bottom layer will be named porous layer (PL).

Table 1
Casting solutions compositions and casting conditions of the cellulose acetate membranes.

	Membrane		
	CA-22	**CA-30**	**CA-34**
Casting solution			
Cellulose acetate (wt%)	17.0	17.0	17.0
Acetone (wt%)	61.0	53.0	49.0
Formamide (wt%)	22.0	30.0	34.0
Film casting conditions			
Temperature of casting solutions (ºC)	20-25		
Temperature of atmosphere (ºC)	20-25		
Solvent evaporation time (min)	0.5		
Medium Gelation time (h)	Ice cold water (1-2 h)		

2.2. Permeation experiments

Permeation experiments were performed to characterize the membranes in terms of pure water hydraulic permeability (L_p (kg.h^{-1}.m^{-2}.bar^{-1})), molecular weight cut-off (MWCO, (kDa)) and salts rejections. The ultrafiltration set-up was previously described by Afonso and de Pinho [19].

The membrane flat plate cells have two detachable parts separated by a porous plate (membrane support), with a membrane surface area of 13.2×10^{-4} m^2.

Before the permeation experiments, the membranes were compacted for 2 h with deionized water at a transmembrane pressure (ΔP) of 3 bar. The hydraulic permeability is obtained by the slope of the straight line of pure water permeate fluxes (J_{pw} (kg.h^{-1}.m^{-2})) as a function of the transmembrane pressure (bar):

$$L_p = \frac{J_{pw}}{\Delta P} \quad (1)$$

The transmembrane pressure used was varied from 1 to 3 bar with a feed flow rate of 180 L.h^{-1}.

The MWCO, defined by the molecular weight of a determined macromolecule whose rejection is higher than 90.9%, was determined from the rejections of organic solutes, using several polyethylene glycol (PEG) and Dextran solutions. The apparent rejection coefficient to solute A, f_A, is defined as:

$$f_A = \frac{C_{Af} - C_{Ap}}{C_{Af}} \quad (2)$$

where C_{Af} and C_{Ap} are the solute A concentrations in the bulk of the feed solution and in the permeate solution, respectively.

To determine the MWCO, the curve of $log(f_A/(1-f_A))$ as a function of the molecular weight of the reference organic solutes (PEG 1000, 3000, 6000, 8000, 10000, 20000 Da; Dextran 70000 Da) was used. The MWCO value is obtained by the intersection of this curve with the 90.9% rejection line ($log\left(\frac{f_A}{(1-f_A)}\right)$=1). The stabilization time for each experimental run was 30 min. The organic solutes concentrations in feed and permeate solutions were determined in terms of total organic carbon (TOC) content, using a Dohrmann Total Organic Carbon Analyzer Model DC-85A.

For the salts rejections experiments, chloride and sulphate salts with three different cations were used, namely NaCl, $CaCl_2$, $MgCl_2$, Na_2SO_4, $CaSO_4$ and $MgSO_4$. The permeation experiments were carried out at 600 ppm of salts, with a feed flow rate of 180 Lh^{-1} at 1 bar and after 30 min of stabilization. The salts concentration determination was performed by conductivity measurements using a Crison GLP 32 conductivity meter.

2.3. Average pore size at the top surface of the membranes active layer

The membrane selective character to a given solute A leads to the development of a concentration profile of this solute from C_{Am} at the membrane/feed interface to C_{Af} at the feed bulk. Whereas the apparent rejection coefficient, f_A, defined by Eq. 2 is based on C_{Af}, an intrinsic rejection coefficient, f'_A, based on C_{Am} is defined by:

$$f'_A = \frac{C_{Am} - C_{Ap}}{C_{Am}} \quad (3)$$

Through the film theory the two rejection coefficients can be related by [20]:

$$f_A = \frac{f'_A}{f'_A + (1 - f'_A)\exp(J_v/k)} \quad (4)$$

Where J_v is the permeate flux and k is the mass transfer coefficient. The latter is estimated by a mass transfer correlation that is case specific to the permeation cell geometry [21, 22]:

$$Sh = 1.5 \times 10^4 Re^{0.42} Sc^{0.33} Lp^{+0.35} \quad (5)$$

The Sherwood number, $Sh = kR_m/D_{AW}$, is correlated to the

Reynolds number $Re = \rho\langle v_c\rangle R_m/\mu$, the Schmidt number, $Sc = \mu/(D_{Aw}\rho)$, and a dimensionless permeability, $Lp^+ = Lp/R_m$, where L_p *and* R_m *(membrane cell radius) are expressed in meters,* D_{Aw} the solute A diffusion coefficient in water ($m^2.s^{-1}$), ρ the density ($kg.m^{-3}$), μ the viscosity ($kg.m^{-1}.s^{-1}$) and $\langle v_c\rangle$ the average feed velocity given by $\langle v_c\rangle = 1.723 \times 10^4 q$. The average velocity expressed in $m.s^{-1}$ and the feed flow rate, q, expressed $m^3.s^{-1}$, are specific of the geometry and flow characteristics of the permeation cell [21, 22]. Based on the fundamental assumptions of the transport models of Deen [23], Tam et al. [24, 25] and Rosa et al. [26], the prediction of intrinsic rejection coefficient is given by:

$$f_A' = 1 - \frac{W}{1-(1-W)e^{-Pe}} \quad (6)$$

where W is the hindrance factor to convection and the Peclet number, Pe, is defined as a function of the average pore radius, $\overline{R_p}$, of the active layer surface:

$$Pe = \frac{W\Delta P\overline{R_p^2}}{8H\mu D_{AW}}\frac{J_v}{J_{pW}} \quad (7)$$

where H is the steric hindrance for diffusion.

The W and H hindrances to convection and to diffusion, respectively, are calculated following the correlations of Bungay and Brenner as referred by Rosa [22].

For ultrafiltration membranes where convective transport is dominant, the Peclet number is very large ($Pe >> 1$), and Eq. 6, simplifies to:

$$f_A' = 1 - W \quad (8)$$

The determination of the UF membranes average pore radius was carried out using an iterative methodology depicted in Figure 2. This methodology developed by Rosa et al. [22, 26] calculates the intrinsic rejection coefficients, $f_{A'exp.}$, taking into account the experimental apparent rejection coefficients of the reference solutes and the quantification of the concentration polarization (Eq. 4), and, on the other hand, calculates a theoretical intrinsic rejection coefficient, $f_{A'calc.}$, based on equations 6 and 7. The least squares algorithm is used to minimise the objective function, $\sum(f_{A'exp.} - f_{A'calc.})^2$, yielding the average mean pore radius, $\overline{R_p}$, at the membrane active layer surface.

The calculation of $f_{A'calc.}$ by Eqs. 6 and 7 requires the use of the physio-chemical properties of the reference solutes presented in Table 2.

Table 2
Physico-chemical properties, Diffusivity and Solute Radius of the reference organic solutes, PEG and Dextran.

Solute	Diffusivity, D_{Aw} ($m^2\,s^{-1}$)	Solute Radius (Å)
PEG 1000	3.06×10^{-10}	7.99
PEG 3000	1.74×10^{-10}	14.10
PEG 6000	1.22×10^{-10}	19.99
PEG 8000	1.06×10^{-10}	23.10
PEG 10000	9.44×10^{-11}	25.90
PEG 20000	6.65×10^{-11}	36.80
Dextran 40000	$5.47\times x10^{-11}$	44.67

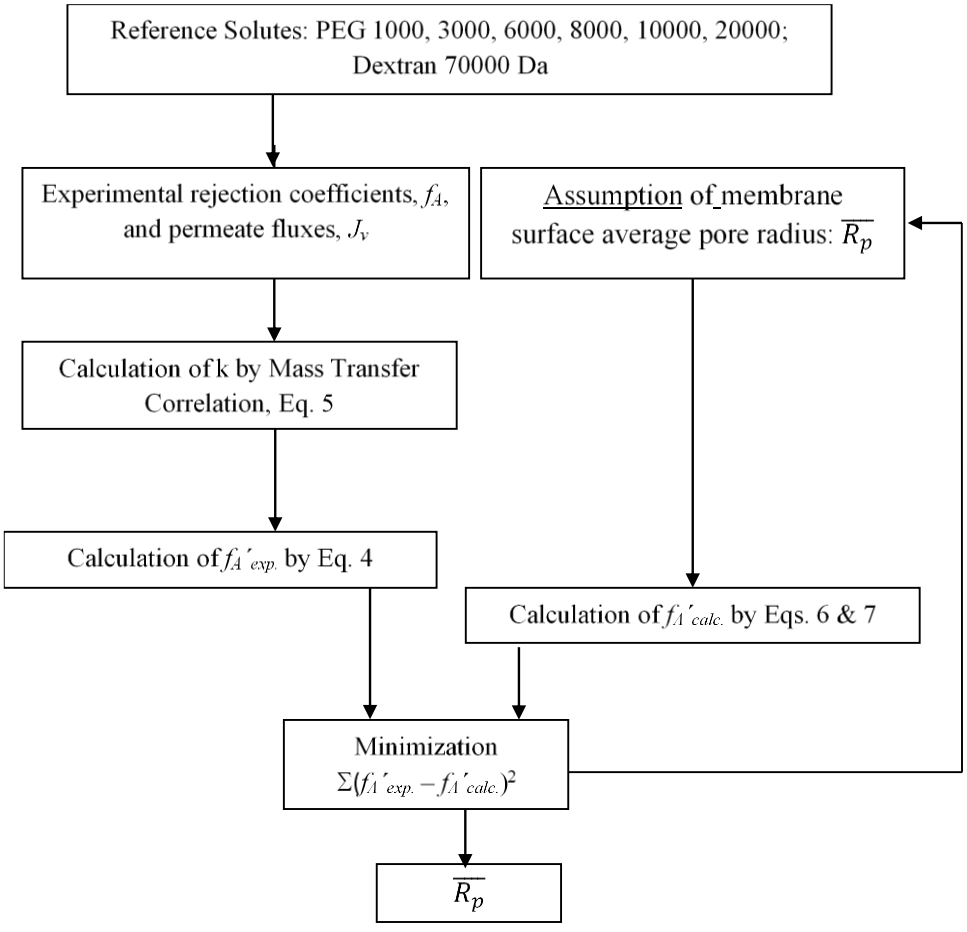

Fig. 2. Scheme of the iterative methodology used to determine the UF membrane average pore radius, $\overline{R_p}$, at the fluid/membrane interface.

2.4. Infrared analysis

Both surfaces of all the asymmetric membranes were analyzed by infrared spectroscopy in attenuated total reflection (ATR) mode. The membranes were kept in water that was periodically renewed, in order to eliminate any residual solvents. Prior to characterization, the excess surface water was removed with an absorbing smooth paper. The membranes were cut in the appropriate dimensions, and placed on a ZnSe ATR crystal (4 mm thick and 80 mm long), with 10 reflections and an incidence angle of 45º. Conditions for an "ideal contact" between the sample and the crystal were guaranteed by carefully adjusting the sample holder lid, so that the band intensities were reproducible [27]. The spectra were scanned in a Mattson RS1 FTIR spectrometer, equipped with a wide band MCT detector (400 to 4000 cm^{-1}), at 4 cm^{-1} resolution, using a horizontal Pike Technologies (HATR) accessory. They were obtained by the ratio of 500 single-beam scans of the sample to the same number of background (clean ATR crystal) scans. The spectra were transformed to $\log_{10}(1/R)$ using the FIRST software and are presented without baseline or smooth corrections.

3. Results and discussion

3.1. Membrane permeation properties

The hydraulic permeabilities of CA-22, CA-30 and CA-34 membranes and the corresponding apparent rejection coefficients (f_A) to neutral solutes of increasing molecular weight are displayed in Table 3.

The membranes average pore radius at the fluid/membrane interface was estimated following the methodology described in Figure 2, using the data presented in Table 3, and the results are summarized in Table 4. The molecular weight cut-off of the membranes obtained following the methodology described in section 2.2 is also presented in Table 4.

Table 3
Hydraulic permeability (L_p) and apparent rejection coefficients to reference solutes (f_A) of CA-22, CA-30 and CA-34 membranes.

Membrane	L_p kg.m^{-2}.h^{-1}.bar^{-1}	f_A (%)						
		PEG (Da)						Dextran (Da)
		1000	3000	6000	8000	10000	20000	DT4000
CA-22	3.5	57.6	84.9	95.9	99.3	-	-	-
CA-30	32.0	-	42.4	73.9	-	89.0	93.5	95.1
CA-34	81.0	-	24.5	48.0	-	63.3	86.4	95.5

Table 4
Average pore radius ($\overline{R_p}$) at the membrane active layer surface and molecular weight cut-off (MWCO) of CA-22, CA-30 and CA-34 membranes.

Membrane	$\overline{R_p}$ (nm)	MWCO (kDa)
CA-22	2.1	4.17
CA-30	2.8	8.32
CA-34	4.5	31.43

As Table 4 shows, the MWCO of the membranes increases strongly with the increase of the average surface pore size of the membranes.

The mass transfer coefficients of the organic reference solutes were estimated through Eq. 5 and the fact that they display very large values (Table 5) renders the values of the intrinsic rejection coefficients, given by Eq. 4, very close to the corresponding values of the experimental apparent rejection coefficients (see Table 3). This efficiency of mass transfer from the membrane/feed interface to the feed bulk means the minimization of concentration polarization and can be attributed to the feed flow conditions.

The apparent rejection coefficients to salts are presented in Figure 3.

The three membranes, CA-22, CA-30 and CA-34, with hydraulic permeabilities of 3.5, 32.0 and 81.0 kg.m^{-2}.h^{-1}.bar^{-1}, respectively, have very different and increasing convective permeation capabilities. The UF membranes are usually associated to negligible rejection coefficients to salts. In fact, this is verified for the two more permeable membranes, CA-30 and CA-34. This is in contrast with the selective permeation pattern of the CA-22 membrane. It displays rejection coefficients equal or higher than 50% for the sulphate salts (Na_2SO_4, $CaSO_4$ and $MgSO_4$) and a lower range of variation, between 14 and 18%, for the chloride salts (NaCl, $CaCl_2$ and $MgCl_2$). According to Eq. 8, for the CA-22 membrane there is differentiation of hindrance factors to convection for these two groups of salts. The membrane/water interactions and its dependence on the membrane polymeric porous structure were assessed by ATR-FTIR analysis and correlated to the salts permeation results.

3.2. ATR-FTIR Analysis

The ATR-FTIR spectra of the active and porous layers of the CA-22, CA-30 and CA-34 asymmetric membranes are compared in Figures 4 and 5, respectively.

Table 5. Mass transfer coefficients and intrinsic rejection coefficients.

Membrane	(Da)	PEG 1000	PEG 3000	PEG 6000	PEG 8000	PEG 10000	PEG 20000	DT 40000
CA-22	k (m.s^{-1})	1.52×10^{-5}	1.04×10^{-5}	8.23×10^{-6}	7.46×10^{-6}	-	-	-
	f_A'	58.4%	85.6%	96.2%	99.3%	-	-	-
CA-30	k (m.s^{-1})	-	2.26×0^{-5}	1.79×10^{-5}	-	1.50×10^{-5}	1.19×10^{-5}	1.04×10^{-5}
	f_A'	-	-	88.5%	-	95.0%	97.6%	99.3%
CA-34	k (m.s^{-1})	-	-	-	-	2.08×10^{-5}	1.64×10^{-5}	1.44×10^{-5}
	f_A'	-	-	-	-	72.6%	90.6%	97.0%

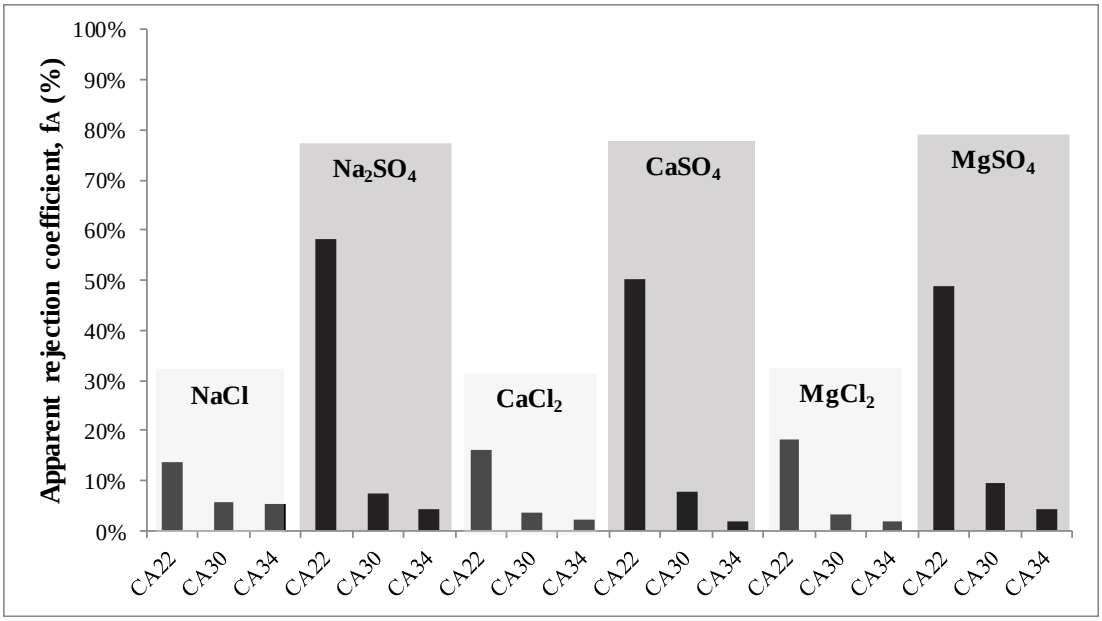

Fig. 3. Salts apparent rejection coefficients for CA-22, CA-30 and CA-34 membranes.

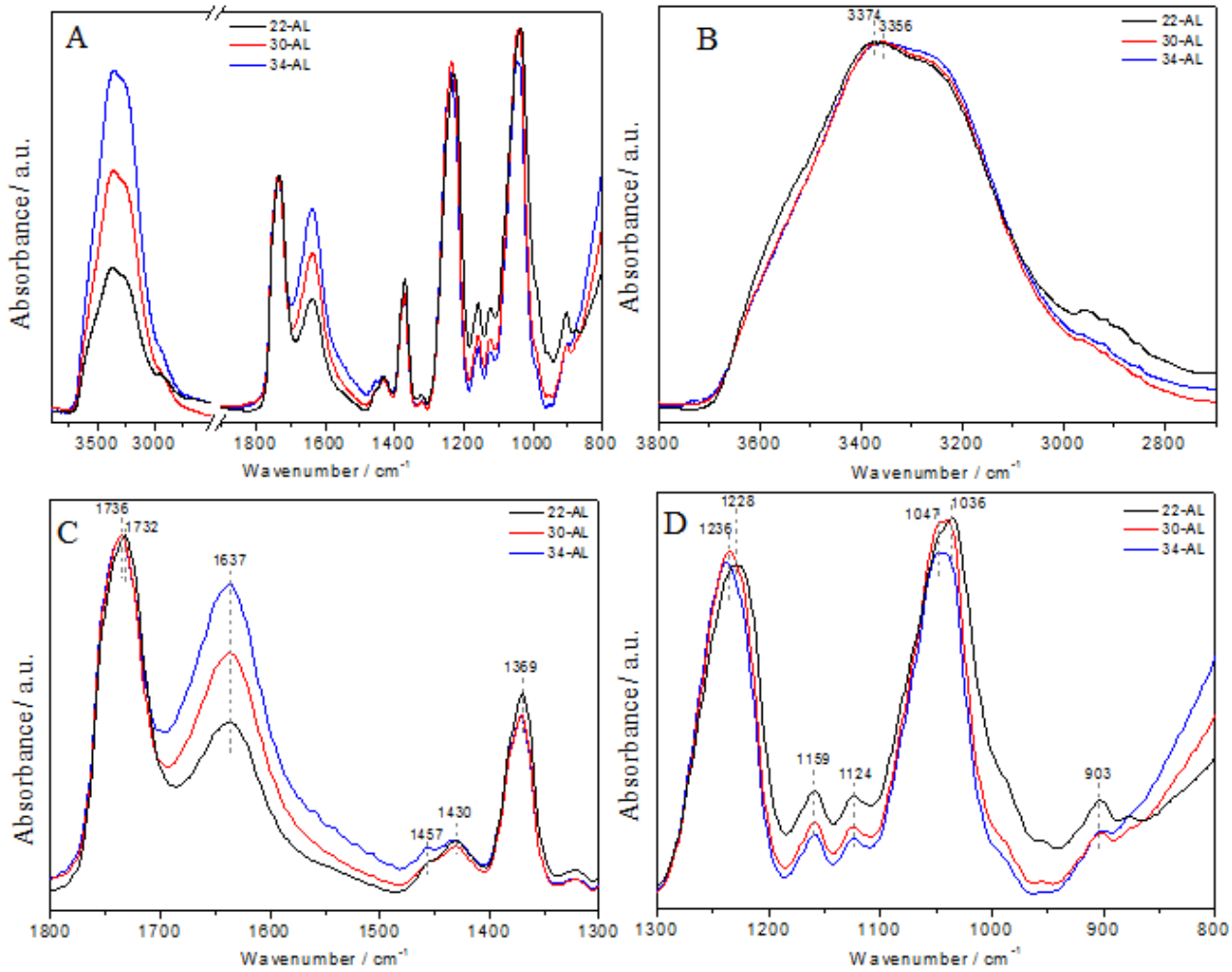

Fig. 4. ATR spectra of the active layer (AL) of CA membranes: (A) complete spectrum, normalized to the C=O stretching band; (B) enhanced 2700-3800 cm^{-1} region, normalized to the maximum of the OH stretching band; (C) enhanced 1300-1800 cm^{-1} region and (D) enhanced 800-1300 cm^{-1} region, both normalized to the νC=O band.

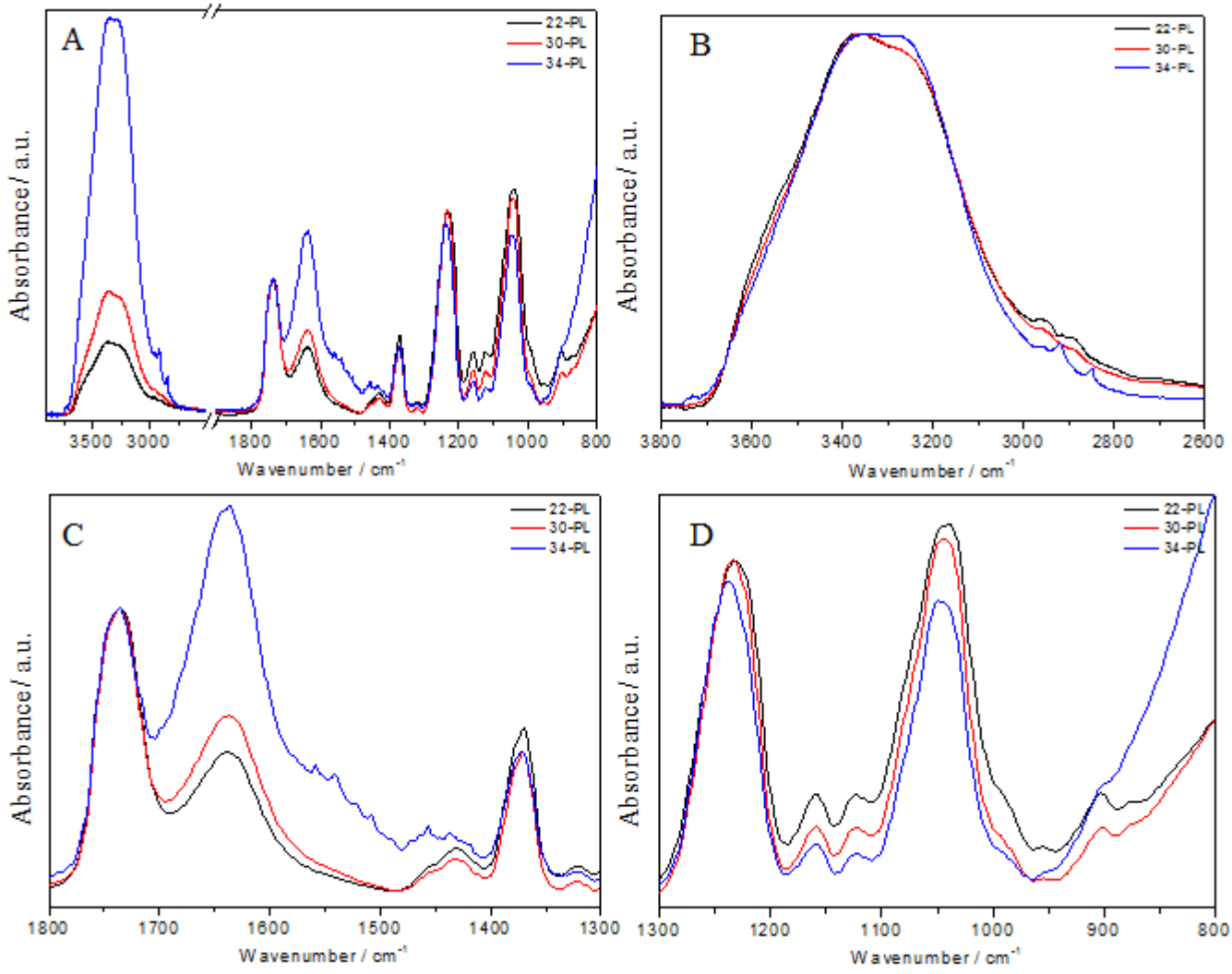

Fig. 5. ATR spectra of the porous layer (PL) of CA membranes: (A) complete spectrum, normalized to the C=O stretching band; (B) enhanced 2700-3800 cm^{-1} region, normalized to the maximum of the OH stretching band; (C) enhanced 1300-1800 cm^{-1} region and (D) enhanced 800-1300 cm^{-1} region, both normalized to the νC=O band.

The complete assignment of the spectra is presented in Table 6, but some comments are pertinent. The broad band centered at ~3400 cm^{-1}, assigned to the OH stretching mode, contains contributions from the hydroxyl groups of non-esterified cellulose (see Figure 1), as well as from adsorbed water, involved in a variety of hydrogen bonds. Since the esterification degree of the cellulose acetate is only 39.8%, the possibility of intramolecular hydrogen bonds between the hydroxyl groups and glycosidic oxygens also exits. Figures 4A and 5A are normalized to the carbonyl band of cellulose acetate and show a clear increase of the relative intensity of the νOH band as the average pore size at the surface of the membrane active layer decreases. In Figures 4B and 5B, normalized to the maximum of this band, it becomes clear that the maximum shifts to lower wavenumbers. Although this is a composed band, the maximum at 3374 cm^{-1} observed for the active layer of membrane CA-22 suggests that the predominant hydrogen bonding interactions are slightly weaker than at the active layers of CA-30 and CA-34, where the maxima were observed at 3359 and 3356 cm^{-1}, respectively. The latter value is indeed more similar to that reported for bulk water (3340 cm^{-1}) [4]. Additionally, the component at ~3200 cm^{-1}, corresponding to hydroxyl groups more strongly hydrogen-bonded, increases with the increase of the average pore size at the surface of the membrane active layer. This is more evident for the porous layer of membrane CA-34. It appears that stronger hydrogen bonds between water molecules or water and cellulose OH groups, similar to "stretched" water [28, 29], gain importance as the surface pore size increases. Previous studies on cellulose acetate membranes based only on the analysis of the OH stretching band reported that the amount of adsorbed water at the membrane active layer and the extent of water-water interactions depend on the surface morphology, both increasing with the membrane surface average pore size [4, 11]. The present observations are consistent with those conclusions. The water deformation mode, centered at 1637 cm^{-1}, is extremely useful to analyze the adsorbed water, because it is the only band unequivocally assignable to water. A quantitative analysis of this band will be presented below.

The CH stretching bands of cellulose acetate are comparatively weak, between 2960 and 2850 cm^{-1}, but are more clearly defined in the porous layer. In the CH deformation region there are a few weak bands and a medium one, typical of the methyl umbrella mode of acetate groups, at 1369 cm^{-1}.

The strong carbonyl stretching mode appears at 1732-1736 cm^{-1}, with the maximum absorption wavenumber almost invariable with the layer or the membrane.

The antisymmetric and symmetric C-O-C stretching modes of the ester appear as strong bands at ~1230 and ~1040 cm^{-1}, respectively. The large shifts that are observed in these bands, from 1228 to 1238 cm^{-1} and from 1036 to 1049 cm^{-1}, respectively, are related to the increase of the membrane surface pore sizes. In fact, the shift to higher wavenumbers corresponds to membranes with increasing active layer surface pore sizes, of 2.1 nm (CA-22), 2.8 nm (CA-30) and 4.5 nm (CA-34), displaying their influence on the conformation of the acetate groups. The weak bands at 1159 and 1124 are also assigned to C-O-C stretching modes, but of the glycosidic bonds and monosaccharide units [30]. The band at 903 cm^{-1} correlates with the acetate methyl groups.

Table 6
Assignments of the ATR-FTIR spectra of CA-22, CA-30 and CA-34 membranes.

Wavenumber/cm^{-1}						
CA-22		**CA-30**		**CA-34**		**Assignment**
Active layer	**Porous layer**	**Active layer**	**Porous layer**	**Active layer**	**Porous layer**	
$3374_{VS, br}$	3373	$3359_{VS, br}$	3359	$3356_{VS, br}$	3356	νOH (H bonded)
$\sim3240_{sh}$	3259	$\sim3240_{sh}$	~3259	$\sim3240_{sh}$	3269	
2958_{vw}	2962	2958_{vw}	2962	2958_{vw}	2958	$\nu_{as}CH_3$
2918_{sh}	-	2918_{sh}	-	2918_{vw}	2918	$\nu_{as}CH_2$
2850_{vw}	-	2850_{vw}	-	2850_{vw}	2851	ν_sCH_3
1732_S	1736	1736_S	1736	1736_S	1736	νC=O
1637_S	1637	1637_S	1637	1637_S	1635	δHOH (H_2O)
1457_w	1456_{sh}	1457_w	1456_{sh}	1457_w	1456	$\delta_{as}CH_3$
1430_w	1431	1430_w	1431	1430_w	1437	δCH_2
1369_m	1371	1369_m	1371	1369_m	1371	δ_sCH_3
1323_{vw}	1321_{vw}	1323_{vw}	1321_{vw}	1323_{vw}	1319_{vw}	γCH_2
1228_{VS}	1232	1234_{VS}	1234	1238_{VS}	1238	ν_{as}COC (acetate)
1159_w	1159	1159_w	1159	1159_w	1159	ν_{as}COC (glycosidic)
1124_w	1122	1124_w	1122	1124_w	1122	ν_{as}COC(glycosidic)
1036_{VS}	1040	1039_{VS}	1045	1047_{VS}	1049	ν_sCOC (acetate)
903_w	903	903_w	903	903_w	901_{sh}	ρCH_3

VS - very strong; S -strong; m - medium; w - weak; vw - very weak; sh - shoulder; br – broad

In order to quantify the water adsorbed at the membranes' surfaces, the intensity ratio between the H-O-H deformation band and one invariant band of the cellulose acetate (the carbonyl stretch) was evaluated. They partially overlap and may have more than one component, because both OH and CO groups may be involved in different hydrogen bonds. The components were identified by a spectral deconvolution in the 1560-1780 cm^{-1} region into a sum of Gaussian profiles, using a non-linear least squares fitting method. The details of the deconvolution are presented in Table S1 (ESI). Four components were retrieved in all the spectra: a very broad one centered at 1638-1639 cm^{-1}, assigned to the water deformation mode in different hydrogen bonds, and three assignable to the carbonyl stretching mode of cellulose acetate, at 1753-1754 cm^{-1}, 1732-1737 cm^{-1} and 1689-1697 cm^{-1}, involved in progressively stronger hydrogen bonds. The water components are not separable, because the hydrogen bonds have smoothly changing energies. For the carbonyl, however, it was possible to estimate the proportion of groups that are freer or more involved in intramolecular hydrogen bonds (as in dry cellulose acetate) [31], by the ratio of areas between the component at 1754 cm^{-1} and the total area of C=O-related components. The results are summarized in Table 7 for the active and porous layers of all the membranes.

It is obvious that the fraction of freer CO groups decreases as the pore size of the membrane increases. However, the differences between the two layers of the same membrane are not significant, which suggests that that fraction correlates more with the average size of the pores than with their content. The involvement of the carbonyl groups in intermolecular hydrogen bonds must be correlated with the capacity of the surfaces to adsorb water, estimated by the ratio between the area of the water deformation band and the added areas of the CO components. These values (last row of Table 7) show that the adsorbed water content increases with the pore size of the membrane. This observation is valid when comparing the active layers of the different membranes, as well as the porous layers. The two layers are very similar in this respect for the denser membranes (CA-22 and CA-30), but for the membrane with larger pores the capacity to adsorb surface water increases significantly in the porous layer.

Table 7
Summary of the spectral deconvolution in the 1560-1780 cm^{-1} region. Relative areas of the water to carbonyl components.

	CA-22				**CA-30**				**CA-34**			
	Active Layer		**Porous Layer**		**Active Layer**		**Porous Layer**		**Active Layer**		**Porous Layer**	
	$\tilde{\nu}$ /cm^{-1}	%A	$\tilde{\nu}$ /cm^{-1}	**%A**	$\tilde{\nu}$ /cm^{-1}	**%A**	$\tilde{\nu}$ /cm^{-1}	**%A**	$\tilde{\nu}$ /cm^{-1}	**%A**	$\tilde{\nu}$ /cm^{-1}	**%A**
Components	1638	35.72	1638	37.13	1638	45.43	1638	44.02	1639	49.85	1639	56.94
	1697	10.80	1696	9.36	1695	8.45	1695	8.44	1693	8.68	1689	12.13
	1732	44.00	1733	43.56	1735	40.55	1735	40.71	1736	37.28	1737	28.48
	1754	9.48	1754	9.95	1754	5.57	1754	6.83	1754	4.20	1753	2.45
$A_{1754}/\Sigma A\nu_{C=O}$	0.15		0.16		0.10		0.12		0.08		0.06	
$A\delta_{HOH}/\Sigma A\nu_{C=O}$	0.56		0.59		0.83		0.79		0.99		1.32	

As a general trend, membranes with larger pores tend to adsorb larger amounts of water that may be hydrogen bonded to other water molecules, the hydroxyl groups of cellulose and the carbonyl groups of the CA, leaving a lower fraction of less bonded CO groups. The porous layer of the membrane with larger pores is the richest in adsorbed water and the poorest in free C=O groups. Since the qualitative information from the OH stretching band (Figures 4A and 5A) is compatible with these findings, a complementary quantitative analysis could bring a new perspective on the nature of the water interactions at the membranes pores. The spectral deconvolution in the region between 2800 and 3700 cm^{-1} into a sum of Gaussian profiles was performed for the active layers, taking into account the possible hydrogen bonds between water molecules, schematized in Figure 6 [32], as well as the contribution from the CA.

The deconvolution results are summarized in Table 8. The proportion of free OH groups decreases as the average pore size at the surface of the membrane increases. Thus, more hydroxyl groups of water are involved in H bonds. The main contributions are from DDAA and DA hydrogen bonds, the same types that predominate in liquid water at room temperature [32]. These components gain relevance as the pore size of the membrane increases, which shows that the water within the pores becomes more similar to liquid water. In fact, since the water content increases with the pore size of the membrane (last row of Table 7), it is understandable that its structure becomes more liquid-water-like. Water may form clusters or even liquid-like structures within mesopores. If CA-34 has larger mesopores, they may accumulate larger amounts of "liquid" water, which is consistent with the relative areas estimated from the ATR spectra. The average pore size of CA-34 (R_p=4.5 nm) is slightly higher than the dimensions of the water clusters formed by 280 molecules with DDAA H bonds between them (~3 nm in diameter) [33], observed in water nanodrops [34] or encapsulated within cavities [35].

On the other hand, these clusters contain hydroxyl groups at the surface, available for hydrogen bonding with carbonyl groups. This also explains the values found for the relative area of freer C=O groups, which decreases from CA-22 to CA-30 and CA-34.

3.3. Convective permeation of salts

As discussed in section 3.1 the high values of the mass transfer coefficients support the assumption of negligible concentration polarization and therefore the resemblance of the salts apparent rejection coefficients to the corresponding intrinsic rejection coefficients. Furthermore, considering that the UF membrane transport is dominated by convection, the results of negligible rejection coefficients to salts presented by the membranes CA-30 and CA-34 lead to the conclusion that they allow unhindered convection. This can be attributed to their large pore sizes and the capacity of accommodating water in liquid-like structures as the infrared results demonstrate (Tables 7 and 8). In contrast, the CA-22 membrane that has the smallest pore size displays hindrances to the salt convective transport, reflected by the rejection coefficients to sulphates around 50% and to chlorides around 15%. The fact that these membranes have, at the polymer/fluid interfaces, more free CO groups and a larger fraction of free water OH-groups enables the establishment of H bonding with solutes and, in the present situation, preferential interaction with sulphate ions (Figure 7).

This is clear from Figure 8, where the intrinsic rejection coefficients are represented as a function of the free carbonyl fraction ($A_{1754}/\Sigma A\nu_{C=O}$).

Sandoval-Olvera et al. [36] modified polyvinylidene fluoride (PVDF) UF membranes, through a plasma treatment, to achieve moderate retentions of anionic species. In the present work, the versatility of the phase inversion method allows the casting of integrally skinned CA membranes that reject salts and differentiate two classes of anions upon their capacity of H bonding.

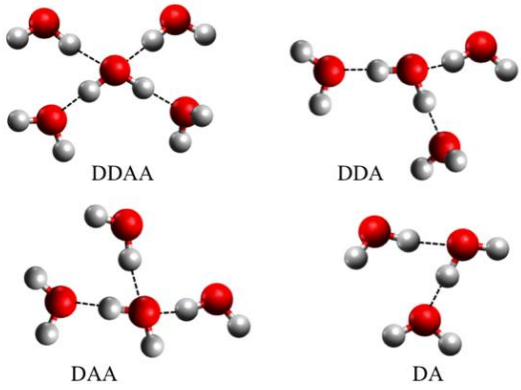

Fig. 6. Schematic representation of hydrogen bonds between water molecules: D stands for hydrogen donor and A for hydrogen acceptor.

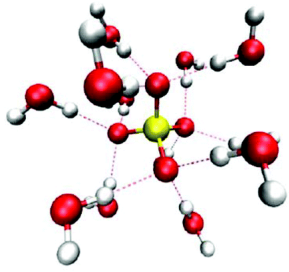

Fig. 7. Schematic representation of a hydrated sulphate ion.

Table 8
Summary of the spectral deconvolution for the active layers in the 2800-3700 cm^{-1} region. Relative areas of the CA and water hydroxyl components.

	CA-22		CA-30		CA-34		
Components	$\tilde{\nu}$ /cm^{-1} [2952]	%A [7.99]	$\tilde{\nu}$ /cm^{-1} [2972]	%A [7.38]	$\tilde{\nu}$ /cm^{-1} [2972]	%A [6.79]	**Tentative assignment** [νCH_3]
	3043	0.36	3038	0.22	3040	0.40	νOH(DAA)
	3097	2.05	3090	1.78	3094	2.08	Overtone
	3239	43.23	3225	40.63	3220	37.37	νOH(DDAA)
	3410	31.73	3400	37.21	3398	42.26	νOH(DA)
	3505	4.87	3511	5.36	3519	4.87	νOH (CA) [**Error! Bookmark not defined.**]
	3569	7.38	3573	5.38	3578	4.25	νOH(DDA)
	3628	2.41	3630	2.04	3630	1.77	νOH(free)
$A\nu OH_{CA}/\Sigma A\nu OH$ (%)	5.4		5.7		5.4		
$A\nu OH_{free}/\Sigma A\nu OH_{H2O}$ (%)	2.8		2.4		2.1		
$\Sigma A\nu OH_{DDAA+DA}/\Sigma A\nu OH_{H2O}$ (%)	88.1		90.8		92.5		

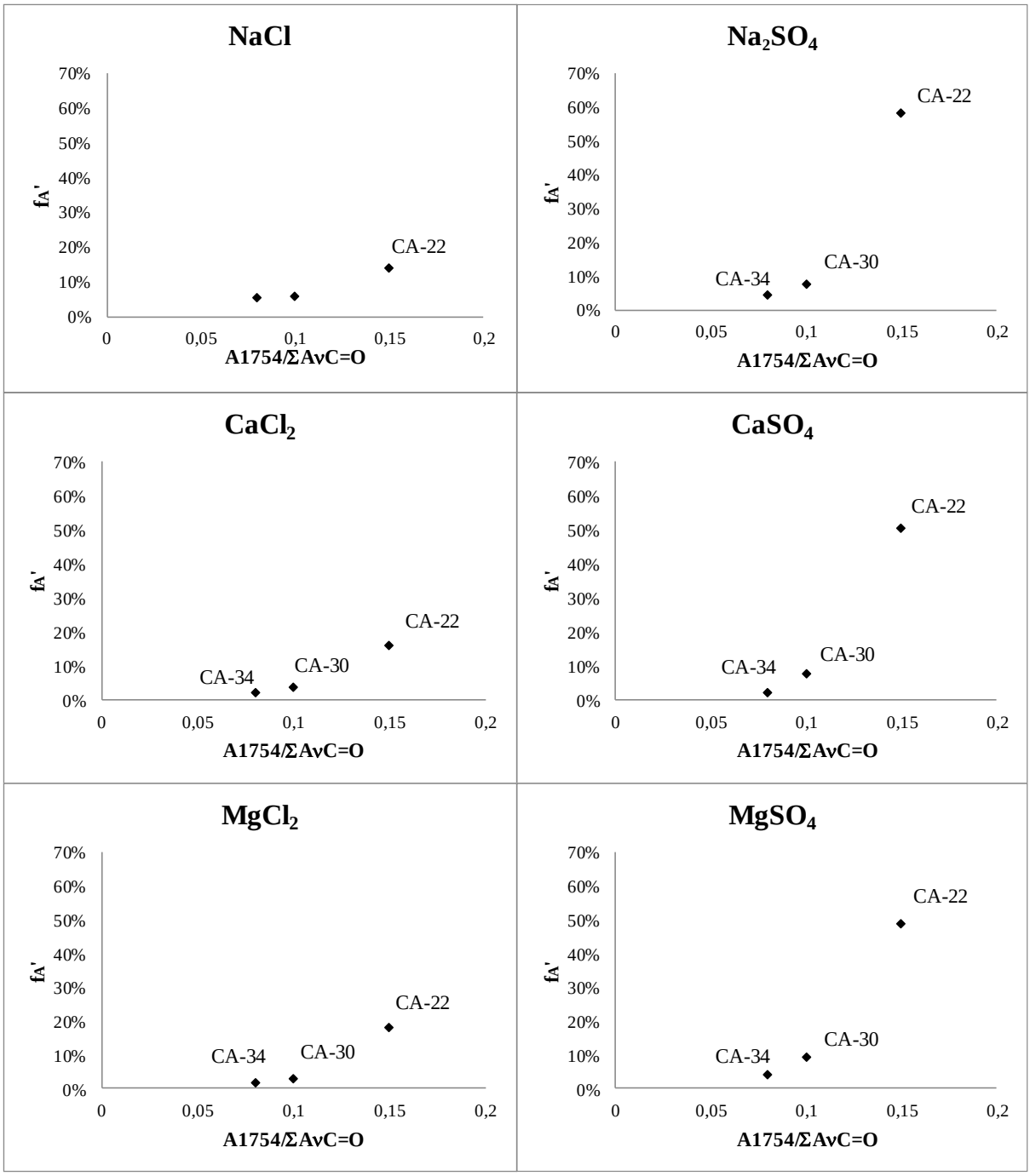

Fig. 8. Variation of the salts intrinsic rejection coefficients, f_{A}', with the $A_{1754}/\Sigma A_{\nu C=O}$ ratio for each of the membranes studied.

4. Conclusions

In the present work the phase inversion method was used to cast three integral asymmetric CA membranes, CA-22, CA-30 and CA-34, with hydraulic permeabilities of 3.5, 32.0 and 81.0 $kg.m^{-2}.h^{-1}.bar^{-1}$, respectively, and with MWCOs of 4.17, 8.32 and 31.43 kDa, respectively.

Regarding salts rejection the CA-30 and CA-34 membranes present very low values for all salts, but the membrane with lower MWCO, CA-22, displays rejection coefficients higher than 50% for the sulphate salts and lower than 20% for the chloride salts. This result is not characteristic of UF membranes and shows that there is a differentiation of hindrance factors to convection for these two types of salts, which was correlated to the membrane surface characteristics assessed by ATR-FTIR analysis.

The ATR-FTIR analysis of the membranes surfaces proved that as the membrane pore sizes increase also increase the hydroxyl water groups involved in strong hydrogen bonds, with liquid-water-like structures (mostly DDAA and DA), concurrently with a larger fraction of strongly bonded CO groups from the polymer. In the case of the UF CA-22 membrane, a larger fraction of free OH and CO free may establish numerous H bonds with the solute, namely with hydrated sulphate ions. Thus, the capability for differentiating anionic species is enabled, like in NF membranes, but with the advantage of having higher permeation fluxes.

Acknowledgments

The authors are grateful to FCT – Fundação para a Ciência e Tecnologia, Portugal – for the finantial support: CeFEMA UID/CTM/04540/2013; UID/NAN/50024/2013; Project PTDC/CTM-Bio/6178/2014.

Electronic Supporting Information

Table S1
Deconvolution results of the 1560-1780 cm^{-1} region of the ATR spectra of CA membranes in a sum of Gaussian components.

CA-22	Active Layer			Porous Layer		
	$\tilde{\nu}$ /cm^{-1}	FWHM/cm^{-1}	% A	$\tilde{\nu}$ /cm^{-1}	FWHM/cm^{-1}	% A
	1638	65.12	35.72	1638	64.18	37.13
	1697	48.03	10.80	1696	48.53	9.36
	1732	35.89	44.00	1733	35.25	43.56
	1754	20.53	9.48	1754	20.28	9.95
$A_{1754}/\Sigma A_{\nu C=O}$	0.15			0.16		
$A_{\delta HOH}/\Sigma A_{\nu C=O}$	0.56			0.59		
CA-30	**Active Layer**			**Porous Layer**		
	$\tilde{\nu}$ /cm^{-1}	FWHM/cm^{-1}	%Area	$\tilde{\nu}$ /cm^{-1}	FWHM/cm^{-1}	% Area
	1638	66.74	45.43771	1638	65.90317	44.02
	1695	45.27	8.44755	1695	45.84119	8.44
	1735	36.70	40.54815	1735	35.64193	40.71
	1754	17.73	5.5666	1754	18.676	6.83
$A_{1754}/\Sigma A_{\nu C=O}$	0.10			0.12		
$A_{\delta HOH}/\Sigma A_{\nu C=O}$	0.83			0.79		
CA-34	**Active Layer**			**Porous Layer**		
	$\tilde{\nu}$ /cm^{-1}	FWHM/cm^{-1}	% Area	$\tilde{\nu}$ /cm^{-1}	FWHM/cm^{-1}	% Area
	1639	65.35	49.85	1639	59.53	56.94
	1693	44.90	8.68	1689	48.47	12.13
	1736	37.82	37.28	1737	37.84	28.48
	1754	16.69	4.20	1753	15.30	2.45
$A_{1754}/\Sigma A_{\nu C=O}$	0.08			0.06		
$A_{\delta HOH}/\Sigma A_{\nu C=O}$	0.99			1.32		

References

[1] S. Loeb, S. Sourirajan, Sea water demineralisation by means of an osmotic membrane, Adv. Chem. Ser. 38 (1963) 117-132. In: Saline Water Conversion-II, R.F. Gould (Ed.), Chap. 9, ACS Editorial Library, Washington DC, USA.

[2] T. Matsuura, S. Sourirajan, Fundamentals of reverse osmosis, National Research Council Canada, Ottawa, Chap. 3 (1985) 165.

[3] R.E. Kesting, Synthetic polymeric membranes - A structural perspective, 2nd ed., Wiley, New York, 1985.

[4] D. Murphy, M.N. de Pinho, An ATR-FTIR study of water in cellulose acetate membranes prepared by phase inversion, J. Membr. Sci. 106 (1995) 245-257.

[5] H.G. Burghoff, W. Pusch, Characterisation of water structure in cellulose acetate membranes by calorimetric measurements, J. Appl. Polym. Sci. 23 (1979) 473-484.

[6] Y. Taniguchi, S. Horigome, The state of water in cellulose acetate membranes, J. Appl. Polym. Sci. 19 (1975) 2743-2748.

[7] C. Toprak, J.N. Agar, M. Falk, State of water in cellulose acetate membranes, J. Chem. Soc., Faraday Trans. 1, 75 (1979) 803-815.

[8] W.A.P. Luck, D. Schioberg, U. Siemann, Infrared investigation of water in desalination membranes, J. Chem. Soc., Faraday Trans. 2, 76 (1980) 136-147.

[9] W.A.P. Luck, Contribution to the desalination membrane mechanism by studies of interactions in aqueous solutions and in polymer hydration, Desalination 62 (1987) 19-35.

[10] P.M. Wiggins, R.T. Van Ryan, The solvent properties of water in desalination membranes, J. Macromolec. Sci. Chem. A23 (1986) 875-903.

[11] C.R. Dias, M.J. Rosa, M.N. de Pinho, Structure of water in asymmetric cellulose ester membranes - an ATR-FTIR study, J. Membr. Sci. 138 (1998) 259-267.

[12] D.F. Stamatialis, C.R. Dias, M. N. de Pinho, Atomic force microscopy of dense and asymmetric cellulose-based membranes, J. Membr. Sci. 160 (1999) 235-242.

[13] D.F. Stamatialis, C.R. Dias, M.N. de Pinho, Structure and permeation properties of cellulose esters asymmetric membranes, Biomacromolecules 1 (2000) 564-570.

[14] A.S. Michaels, New separation technique for the CPI, Chem. Eng. Prog. 64 (1968) 31.

[15] M.M. Rohani, A. Zidney, Role of electrostatic interactions during protein ultrafiltration, Adv. Colloid Interf. Sci 160 (2010) 40-48.

[16] M. Hadidi, A. Zidney, Analysis of the effects of electrostatic interactions on protein transport through zwitterionic ultrafiltration membranes using protein charge ladders, J. Appl. Polym. Sci. 132 (2015) 41540.

[17] J. Puls, S.A. Wilson, D. Hölter, Degradation of Cellulose Acetate-Based Materials: A Review, J. Polym. Environ. 19 (2011) 152-165.

[18] B. Kunst, S. Sourirajan, An approach to the development of cellulose acetate ultrafiltration membranes, J. Appl. Polym. Sci. 18 (1974) 3423-3434.

[19] M.D. Afonso, M.N. de Pinho, Ultrafiltration of bleach effluents in cellulose production, Desalination 79 (1990) 115-124.

[20] M. Mulder, Basic Principles of Membrane Technology, Springer, 1996.

[21] A. Giacobbo, A.M. Bernardes, M.J.F. Rosa, M.N. de Pinho, Concentration polarization in ultrafiltration/nanofiltration for the recovery of polyphenols from winery wastewaters, Membranes 8 (2018) 46-57.

[22] M.J.F. Rosa, Separação Selectiva de Compostos Orgânicos de Correntes Aquosas por Ultrafiltração e Nanofiltração. Ph.D. Thesis, Instituto Superior Técnico, Technical University of Lisbon, Lisbon, Portugal, 1995.

[23] W.M. Deen, Hindered transport of large molecules in liquid-filled pores, AIChE J. 33 (1987) 1409-1425.

[24] C.M. Tam, A.Y. Tremblay, Membrane pore characterization - comparison between single and multicomponent solute probe techniques, J. Membrane Sci. 57 (1991) 271-287.

[25] M.D. Guiver, C.M. Tam, Preparation and membrane applications of functional group polysulfones, Proc. Macromolecules, 34th Int. Symp. Macromolecules, Prague, 1992.

[26] M.J. Rosa, M.N. de Pinho, Separation of organic solutes by membrane pressure-driven processes, J. Membr. Sci. 89 (1994) 235-243.

[27] T. Buffeteau, B. Desbat, D. Eyquem. Attenuated total reflection Fourier transform infrared microspectroscopy: Theory and application to polymer samples, Vib. Spectrosc. 11 (1996) 29-36.

[28] C.J. Tainter, Y. Ni, L. Shi, J.L. Skinner, Hydrogen bonding and oh-stretch spectroscopy in water: hexamer (cage), liquid surface, liquid, and ice, J. Phys. Chem. Lett. 4 (2013) 12-17.

[29] P.M. Wiggins. Water structure in polymer membranes, Prog. Polym. Sci. 13 (1988) 1-35.

[30] N.A. Nikonenko, D.K. Buslov, N.I. Sushko, R.G. Zhbankov. Investigation of stretching vibrations of glycosidic linkages in disaccharides and polysaccarides with use of IR spectra deconvolution, Biopolymers 57 (2000) 257-262.

[31] H. Kamal, F.M. Abd-Elrahim, S. Lotfy, Characterization and some properties of cellulose acetate-co-polyethylene oxide blends prepared by the use of gamma irradiation, J. Radiat. Res. Appl. Sci. 7 (2014) 146-153.

[32] Q. Sun, Local statistical interpretation for water structure, Chem. Phys. Lett. 568-569 (2013) 90-94.

[33] O. Loboda, V. Goncharuk, Theoretical study on icosahedral water clusters, Chem. Phys. Lett. 484 (2010) 144-147.

[34] A. Müller, H. Bögge, E. Diemann, Structure of a cavity-encapsulated nanodrop of water, Inorg. Chem. Commun. 6 (2003) 52-53.

[35] M. Garcia-Ratés, P. Miró, J.M. Poblet, C. Bo, J.B. Avalo, Dynamics of encapsulated water inside Mo_{132} cavities, J. Phys. Chem. B 115 (2011) 5980-5992.

[36] I.G. Sandoval-Olvera, P. González-Muñoz, L. Palacio, A. Hernández, M. Ávila-Rodríguez, P. Prádanos, Ultrafiltration membranes modified by PSS deposition and plasma treatment for Cr(VI) removal, Sep. Purif. Technol. 210 (2019) 371-381.